CANCER

A PET imaging approach for determining EGFR mutation status for improved lung cancer patient management

Xilin Sun,[1,2,3] Zunyu Xiao,[1] Gongyan Chen,[4] Zhaoguo Han,[1] Yang Liu,[1] Chongqing Zhang,[1] Yingying Sun,[2] Yan Song,[1] Kai Wang,[1,2] Fang Fang,[2] Xiance Wang,[1] Yanhong Lin,[1] Lili Xu,[5] Liming Shao,[5] Jin Li,[6] Zhen Cheng,[3]* Sanjiv Sam Gambhir,[3]* Baozhong Shen[1,2]*

Tumor heterogeneity and changes in epidermal growth factor receptor (EGFR) mutation status over time challenge the design of effective EGFR tyrosine kinase inhibitor (TKI) treatment strategies for non–small cell lung cancer (NSCLC). Therefore, there is an urgent need to develop techniques for comprehensive tumor EGFR profiling in real time, particularly in lung cancer precision medicine trials. We report a positron emission tomography (PET) tracer, *N*-(3-chloro-4-fluorophenyl)-7-(2-(2-(2-(2-^{18}F-fluoroethoxy) ethoxy) ethoxy) ethoxy)-6-methoxyquinazolin-4-amine (^{18}F-MPG), with high specificity to activating EGFR mutant kinase. We evaluate the feasibility of using ^{18}F-MPG PET for noninvasive imaging and quantification of EGFR-activating mutation status in preclinical models of NSCLC and in patients with primary and metastatic NSCLC tumors. ^{18}F-MPG PET in NSCLC animal models showed a significant correlation ($R^2 = 0.9050$) between ^{18}F-MPG uptake and activating EGFR mutation status. In clinical studies with NSCLC patients ($n = 75$), the concordance between the detection of EGFR activation by ^{18}F-MPG PET/computed tomography (CT) and tissue biopsy reached 84.29%. There was a greater response to EGFR-TKIs (81.58% versus 6.06%) and longer median progression-free survival (348 days versus 183 days) in NSCLC patients when ^{18}F-MPG PET/CT SUV$_{max}$ (maximum standard uptake value) was ≥2.23 versus <2.23. Our study demonstrates that ^{18}F-MPG PET/CT is a powerful method for precise quantification of EGFR-activating mutation status in NSCLC patients, and it is a promising strategy for noninvasively identifying patients sensitive to EGFR-TKIs and for monitoring the efficacy of EGFR-TKI therapy.

INTRODUCTION

Precision medicine is "an emerging approach for disease treatment and prevention that takes into account individual variability in genes, environment, and lifestyle for each person" (*1*). It is becoming a widely recognized approach in the medical field. An important premise of precision medicine is the classification of individuals into subpopulations with different susceptibilities to disease based on genetic, molecular, or cellular profiles. Preventive or therapeutic interventions can then be focused on those individuals who will benefit from them, thereby sparing those who will not benefit from the expense and side effects (*2*). In non–small cell lung cancer (NSCLC), precision medicine is an attractive model for incorporating genomic features into clinical trial design (*3*). A major shift in the approach to NSCLC treatment occurred when it was recognized that tumor epidermal growth factor receptor (EGFR) mutation status determines the effectiveness of treatments with EGFR tyrosine kinase inhibitors (TKIs) (*4*). EGFR-TKIs have since become a mainstay in the treatment of lung adenocarcinomas harboring sensitizing mutations within the EGFR gene (*3*–*5*). The median survival for these patients is now greater than 2 years (*6*, *7*), more than twice the survival of patients receiving only chemotherapy (*8*). The most frequently detected alterations in the EGFR tyrosine kinase domain (exon 19 E746-A750 deletion and exon 21 L858R point mutation) occur in 30 to 50% of Asian NSCLC patients (*9*). In these patients, the overall rate of response to EGFR-TKIs is as high as 80% compared to less than 10% in patients with wild-type EGFR (*10*). Thus, the estimation of EGFR mutation status is essential for the identification of NSCLC patients who may benefit from treatment with EGFR-TKIs and hence for the improvement of prognosis and EGFR-TKI therapy efficacy.

Although several techniques are currently available to assess EGFR mutation status, these methods require biopsied samples and can often fail or have poor reproducibility because of insufficient material for mutation analysis (less than 50% of biopsied samples). In addition, intra- and intertumor heterogeneity over space and time makes it even more challenging to assess EGFR mutation status and use that information for designing effective EGFR-TKI–based therapeutic strategies (*11*–*14*). Plasma samples have been used as surrogate tumor tissue samples to detect EGFR mutation status in patients with NSCLC. However, although this is a less invasive method for detecting genetic alterations, several studies found inconsistencies between the EGFR mutation status estimated from plasma and tumor DNA samples (*15*, *16*). Moreover, plasma samples cannot address the issue of expression heterogeneity in primary or metastatic tumors. Neither biopsies nor plasma samples can provide precise anatomical information such as size, shape, and position of NSCLC tumors, nor their relationship with adjacent structures, although this information is crucial for clinical therapy response evaluation and treatment plan reaffirmation.

---

[1]Molecular Imaging Research Center, Harbin Medical University (MIRC), Harbin, Heilongjiang 150028, China. [2]TOF-PET/CT/MR Center, The Fourth Hospital of Harbin Medical University, Harbin, Heilongjiang 150028, China. [3]Molecular Imaging Program at Stanford (MIPS), Department of Radiology, Stanford University School of Medicine, Stanford, CA 94305, USA. [4]Department of Respiratory Medical Oncology, The Tumor Hospital Affiliated Harbin Medical University, Harbin, Heilongjiang 150049, China. [5]School of Pharmacy, Fudan University, Shanghai 201203, China. [6]College of Bioinformatics Science and Technology, Harbin Medical University, Harbin, Heilongjiang 150081, China.
*Corresponding author. Email: shenbz@ems.hrbmu.edu.cn (B.S.); sgambhir@stanford.edu (S.S.G.); zcheng@stanford.edu (Z.C.)

Molecular imaging with positron emission tomography (PET) shows potential for noninvasively detecting cancer biomarkers in primary or metastatic tumors and therefore for identifying patients who are likely to respond to specific treatments (*17–21*). The development of such techniques could overcome the limitations of current invasive methods, improve NSCLC diagnosis and therapeutic outcome, and may play a role in translating precision medicine into clinical practice (*19*). Here, we report the synthesis of a polyethylene glycol (PEG)–modified (PEGylated) anilinoquinazoline derivative, 2-(2-(2-(2-(4-(3-chloro-4-fluorophenylamino)-6-methoxyquinazolin-7-yl)oxy)ethoxy)ethoxy)ethoxy)ethyl 4-methylbenzenesulfonate (T-MPG), based on the known EGFR-TKI PD153035 (*22*, *23*). T-MPG was then radiolabeled with ^{18}F using a simple one-step method to generate the tracer ^{18}F-MPG. Furthermore, we evaluated the binding specificity of ^{18}F-MPG in NSCLC cultured cells and the feasibility of using ^{18}F-MPG PET for noninvasive imaging and quantification of EGFR-activating mutation status in preclinical models of NSCLC. Here, we present the first-in-human results demonstrating that noninvasive imaging of EGFR-activating mutation status in primary and metastatic tumors with ^{18}F-MPG PET/computed tomography (CT) is a valid strategy for stratifying NSCLC patients for EGFR-TKI treatment. This strategy achieves (i) differentiating of tumor EGFR-activating mutation status in vivo with noninvasive, whole-body PET imaging; (ii) prediction of EGFR-TKI sensitivity/resistance and patient survival; and (iii) monitoring of the dynamic changes in EGFR mutation status during therapy and guidance of precise treatment.

RESULTS

Chemistry and radiochemistry

To test the concept of using ^{18}F-MPG PET/CT strategy for stratifying NSCLC patients for EGFR-TKI treatment (Fig. 1A), we synthesized ^{18}F-MPG. The tosylate precursor T-MPG (compound 9) was prepared by multistep organic synthesis. Nonradioactive F-MPG (compound 13) was also synthesized for use as a standard (fig. S1). ^{18}F-MPG was then successfully prepared by a one-step radiofluorination process through direct nucleophilic substitution of the tosylate precursor T-MPG with ^{18}F-fluoride (Fig. 1B and fig. S2A). At the end of the purification, the radiochemical purity of ^{18}F-MPG was >99%, its specific activity was ~125 gigabecquerel/μmol, and the noncorrected radiolabeling yield was >20% (*n* = 6). ^{18}F-MPG was eluted at a retention time of 22.55 min.

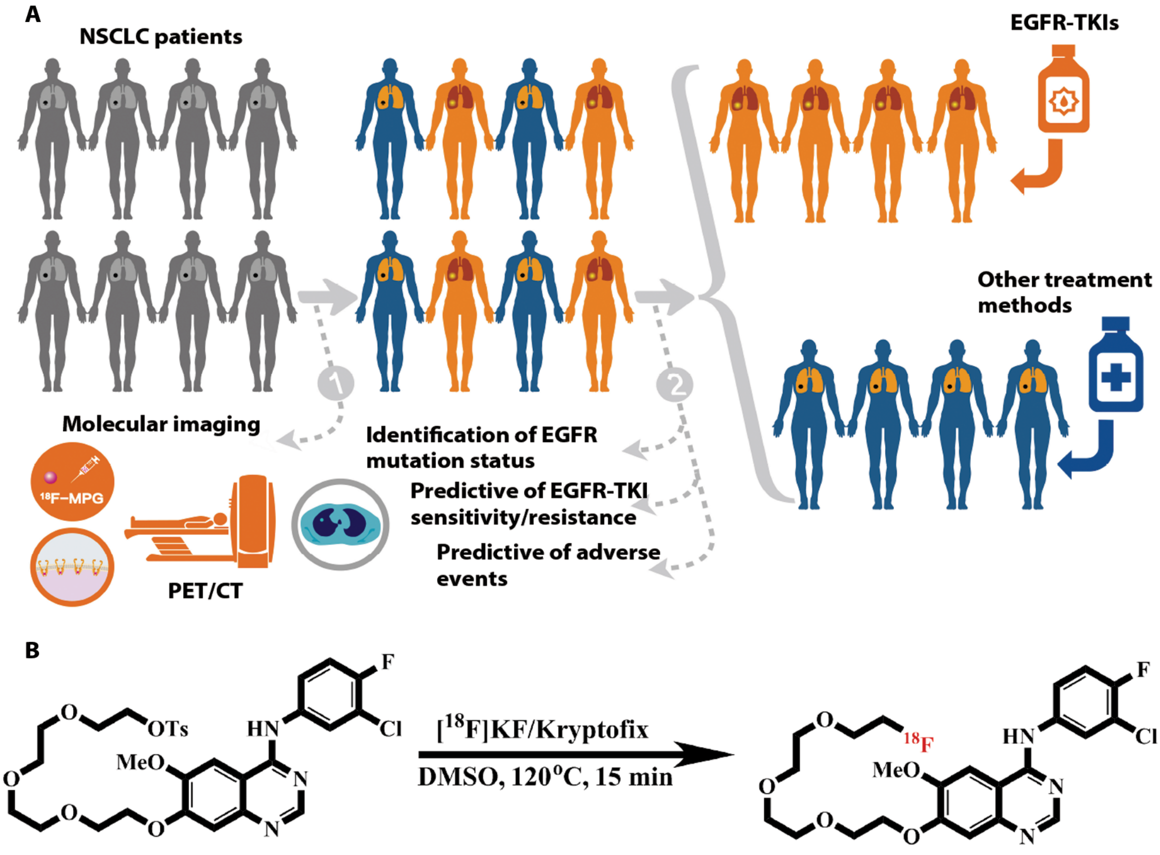

Fig. 1. Molecular imaging of EGFR-activating mutation status for stratification of patients. (**A**) Schematic of epidermal growth factor receptor (EGFR) tyrosine kinase inhibitors (TKIs) explaining the benefits to patients with non–small cell lung cancer (NSCLC) through a stratification strategy using ^{18}F-MPG [*N*-(3-chloro-4-fluorophenyl)-7-(2(2-(2-(2-^{18}F-fluoroethoxy) ethoxy) ethoxy) ethoxy)-6-methoxyquinazolin-4-amine] positron emission tomography (PET)/computed tomography (CT). ^{18}F-MPG selectively binds to tumors expressing the EGFR-activating mutation, such that PET/CT can qualitatively and quantitatively reveal the EGFR mutation expression of tumors. The proposed concept can be eventually translated into clinical use. For patients with NSCLC, especially when the conventional EGFR mutation status test result is ambiguous and biopsies are not feasible or are inconclusive, ^{18}F-MPG PET/CT can serve as a noninvasive, repeatable technique to comprehensively monitoring intra- and intertumor EGFR-activating mutation status in vivo. This strategy can be a valuable diagnostic tool to predict the EGFR-TKI sensitivity/resistance, survival, and guide precision EGFR-TKI treatment. (**B**) Synthesis of ^{18}F-MPG; reagents and conditions: K^{18}F/Kryptofix/dimethyl sulfoxide (DMSO), 120°C, 15 min, 23.79% radiochemical yield.

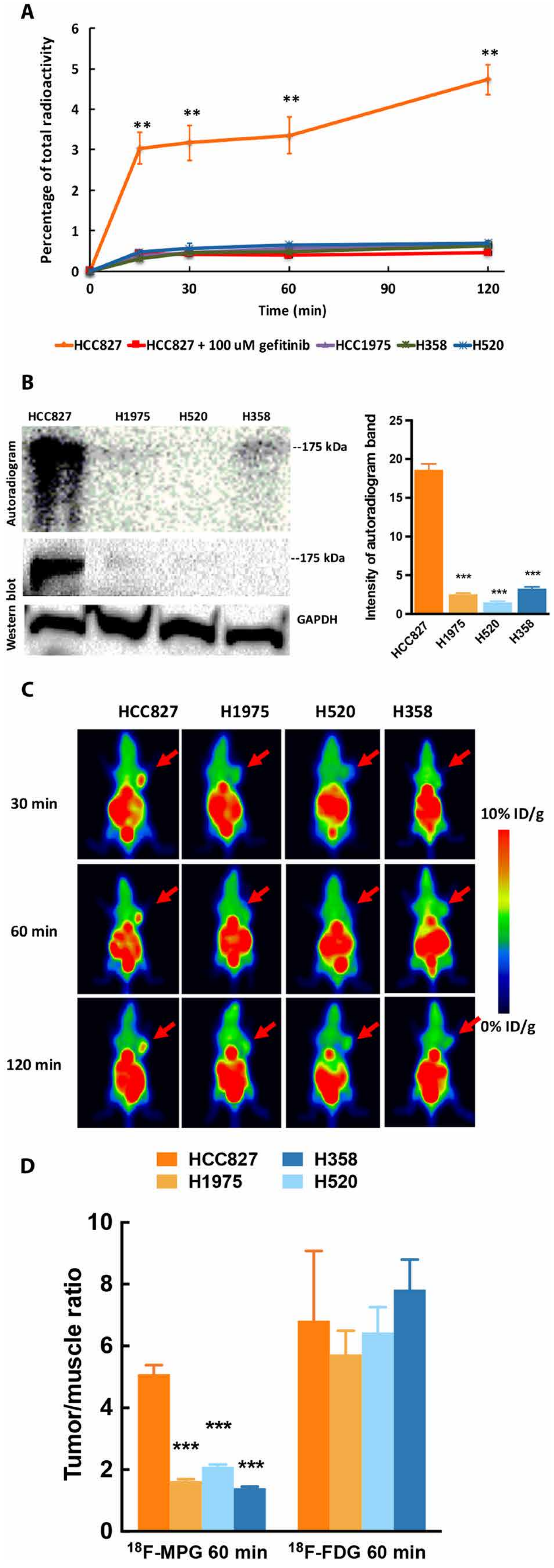

Fig. 2. In vitro and preclinical study with ^{18}F-MPG. (**A**) Quantitative uptake of ^{18}F-MPG in four NSCLC cell lines and pretreatment with gefitinib. Data are means ± SD of three independent experiments. $^{**}P < 0.01$ versus line-matched ^{18}F-MPG uptake in HCC827 cells, Student's *t* test. (**B**) The autoradiography and the same Western blot membrane stained with E746-A750–specific antibody. A single ^{18}F-labeled protein band corresponds to the predominant band of ~175 kDa. Graphs next to the blots show densitometric quantification of autoradiogram band normalized to background. $^{***}P < 0.001$ versus HCC827. GAPDH, glyceraldehyde-3-phosphate dehydrogenase. (**C**) Decay-corrected whole-body coronal PET images of HCC827, H1975, H520, and H358 tumor-bearing mice at 30, 60, and 120 min after injection of 3.7 megabecquerels (MBq; 100 μCi) of ^{18}F-MPG (red arrows indicate the location of the tumors). % ID/g, percentage of injected dose per gram. (**D**) Comparison of tumor/muscle ratios of ^{18}F-MPG and ^{18}F-FDG at 60 min after injection of 3.7 MBq (100 μCi) of tracer in different tumor-bearing mice (*n* = 6 per group) as measured by PET imaging. Data are means ± SD. $^{***}P < 0.001$ versus line-matched ^{18}F-MPG uptake in HCC827 cells, analysis of variance (ANOVA) with the Newman-Keuls multiple comparison test. ^{18}F-FDG uptake versus ^{18}F-MPG uptake in HCC827, ANOVA with the Newman-Keuls multiple comparison test.

In vivo metabolic stability analysis

The in vivo murine metabolic stability assays are shown in fig. S2 (B to E). At 1 hour after injection, 86.84, 96.08, 80.20, and 96.65% of ^{18}F-MPG remained in the tumor, plasma, liver, and urine, respectively. These results demonstrated that ^{18}F-MPG had excellent stability in vivo, suggesting that this PET tracer is suitable for quantitative imaging of EGFR-activating mutations in vivo.

Characterization of NSCLC cell lines and xenografts in mice

Four NSCLC cell lines (HCC827, H1975, H358, and H520) were selected to establish xenografts in mice to assess ^{18}F-MPG PET ex vivo and in vivo. HCC827 and H1975 xenografts both displayed a high degree of EGFR and phosphorylated-EGFR (phospho-EGFR) immunoreactivity. In contrast, in H358 and H520, EGFR and phospho-EGFR immunoreactivity was significantly lower or even undetectable (fig. S3A). EGFR E746-A750del protein was only detectable in HCC827 xenografts by fluorescence staining, and it was undetectable in H1975, H358, or H520 xenografts (fig. S3A). Total EGFR, phospho-EGFR, and EGFR E746-A750del measured by Western blot further demonstrated extensive EGFR activation in HCC827 and its derived xenografts (fig. S3B). Biochemical assays showed that EGFR E746-A750del–expressing HCC827 cells are most sensitive to gefitinib treatment [half maximal inhibitory concentration (IC_{50}) = 3.2 nM], whereas H1975 cells (L858R/T790M EGFR) showed higher resistance to gefitinib (IC_{50} = 12.9 μM). Moreover, H358 and H520 with low EGFR expression and phospho-EGFR reactivity also exhibited high resistance to gefitinib (IC_{50} = 143.8 and 5.6 μM, respectively).

Preferential targeting of ^{18}F-MPG in NSCLC cells with EGFR-activating mutation

To visualize the interaction between ^{18}F-MPG and the EGFR (wild type, 19del-EGFR, and L858R/T790M double mutant) host binding site, we performed molecular docking assays. F-MPG adopted a similar conformation to PD153035 in the binding site (fig. S4). Key and strong interactions remained between the F-MPG quinazoline ring and the surrounding residues, including Met^{793} and Lys^{745} in 19del-EGFR. No strong interactions were detected in wild-type and double-mutant EGFR, whereas different orientations of the 4-PEG side chain were observed.

In vitro biochemical assays were performed to compare the affinity of F-MPG to different EGFR mutants. F-MPG has a 4865-, 2296-, and 2908-fold increased inhibitory activity for EGFR E746-A750del cells when compared to EGFR L858R/T790M, EGFR-negative, or EGFR

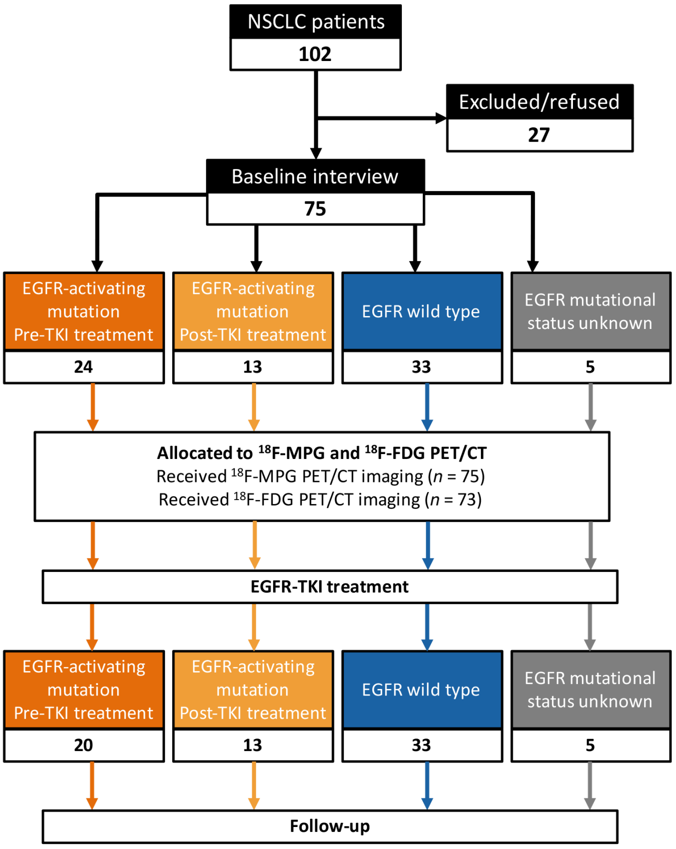

***n* = patients remaining in study**

Fig. 3. Study design and patient allocation. Seventy-five of 102 NSCLC patients were divided into four groups according to EGFR mutation status by gene test result at baseline interview. All patients had participated in the ^{18}F-MPG study, and 73 of 75 patients participated in both the ^{18}F-MPG and ^{18}F-FDG studies. A total of 71 patients received EGFR-TKIs and/or continued to be treated with EGFR-TKIs.

wild-type cells, respectively. These results showed that F-MPG activity was much higher with EGFR-activating mutations than inactive mutant EGFR. The IC$_{50}$ of F-MPG in HCC827, H1975, H520, and H358 was measured to be 0.0044 ± 0.0011 μM, 21.41 ± 1.6777 μM, 10.1027 ± 3.6062 μM, and 12.7970 ± 7.4973 μM, respectively.

To assess targeting specificity of F-MPG analogs for EGFR-activating mutations, HCC827, H1975, H520, and H358 cells were stained with either QD620-conjugated MPG (QD620-MPG) or QD620 alone. QD620-MPG showed abundant binding to HCC827 cells, significantly less binding to H358 cells ($P < 0.01$), and no detectable binding to H1975 or H520 cells (fig. S5A). The control probe, QD620, exhibited minimum binding in all cell lines. Next, the binding specificity of QD620-MPG to EGFR-activating mutations was evaluated. Preincubation with gefitinib (100 μM) abrogated the uptake of QD620-MPG to HCC827 cells (fig. S5B). Flow cytometry analysis confirmed the results: A high fraction of HCC827 cells was labeled with QD620-MPG, whereas a much lower amount of the probe was detected in H1975, H520, or H358 cells (fig. S5C). Similarly, the control probe QD620 failed to detect EGFR-activating mutation status.

In cell uptake assays, ^{18}F-MPG displayed significantly higher cellular uptake in HCC827 cells ($P < 0.01$) than in H1975, H520, and H358 cells at all time points. The maximal uptake of ^{18}F-MPG occurred at 2 hours in HCC827 cells, and it was about eightfold higher than in other NSCLC cells. Moreover, HCC827 cells pretreated with gefitinib showed ~90% lower ^{18}F-MPG uptake than untreated cells (Fig. 2A). Autoradiography confirmed this preferential and selective binding of ^{18}F-MPG to the EGFR-activating mutant kinase (Fig. 2B). The intensity of autoradiography bands in HCC827 cells ($P < 0.001$) was significantly higher than in H520 and H358 cells, and it was barely detectable in H1975 cells expressing EGFR L858R/T790M. The 175-kDa protein bands also reacted with anti-EGFR (E746-A750) antibody (Fig. 2B). These findings demonstrate that ^{18}F-MPG had high specificity for EGFR-activating mutant NSCLC cells.

^{18}F-MPG differentiating EGFR-activating mutation status in vivo

^{18}F-MPG was tested in subcutaneous xenografts of four different NSCLC cell lines ($n = 6$ per group). PET imaging showed rapid and strong accumulation of ^{18}F-MPG in HCC827 tumor xenografts and, to a lesser degree, in H1975, H520, and H358 tumor xenografts at all time points examined (Fig. 2C and tables S1 to S3). ^{18}F-MPG accumulation at 60 min after intravenous injection reached 7.22 ± 0.28% ID/g (percentage of injected dose per gram) in HCC827 tumors. In contrast, ^{18}F-MPG accumulation was significantly lower in H1975, H520, and H358 tumors, reaching 3.93 ± 0.44% ID/g, 3.59 ± 0.93% ID/g, and 4.11 ± 0.46% ID/g, respectively (table S2). Tumor-to-muscle (T/M) ratio of ^{18}F-MPG accumulation at 60 min after intravenous injection reached 5.56 in HCC827 tumors and was 3.41, 2.65, and 3.47 times higher than in H1975, H520, and H358 tumors, respectively ($F_{3,20} = 123.5$, $P < 0.0001$; Fig. 2D). A comparison with ^{18}F-fluorodeoxyglucose (^{18}F-FDG) further confirmed the in vivo EGFR-activating mutation binding specificity of ^{18}F-MPG. ^{18}F-FDG showed higher T/M ratios in all mice xenografts than ^{18}F-MPG. Moreover, no statistically significant difference was found between the T/M ratios of ^{18}F-FDG in HCC827, H1975, H520, and H358 mice xenografts ($F_{3,20} = 0.4199$, $P = 0.7407$; Fig. 2D and table S4). Blocking assays with gefitinib pretreatment in HCC827 xenograft mice ($n = 5$ per group) resulted in a twofold decrease in ^{18}F-MPG accumulation in HCC827 tumors in vivo ($P < 0.01$; fig. S6, A and B), confirming the targeting specificity of ^{18}F-MPG to EGFR-activating mutations.

In biodistribution experiments, mice bearing HCC827, H1975, H358, and H520 xenografts ($n = 6$ per group) were injected with 0.925 megabecquerels (MBq) (25 μCi) of ^{18}F-MPG and then sacrificed 30 min, 1 hour, or 2 hours after injection (tables S5 to S7). Consistent with the PET imaging results, ^{18}F-MPG uptake in HCC827 tumors was significantly higher than in H1975, H520, or H358 tumors ($F_{3,20} = 93.27$, $P < 0.0001$; fig. S6C). The T/M ratios of ^{18}F-MPG calculated from the biodistribution data were also significantly higher in HCC827 tumors than in H1975, H520, and H358 tumors ($F_{3,20} = 31.89$, $P < 0.0001$). Moreover, the T/M ratios of ^{18}F-MPG in HCC827, H1975, H358, and H520 quantified in the biodistribution study and by PET imaging were comparable (tables S1 to S3 and S5 to S7). These results indicated that ^{18}F-MPG selectively targeted human EGFR-activating mutations with high specificity in vivo.

Patient safety and dosimetry of ^{18}F-MPG from the first-in-human study

^{18}F-MPG was found to be safe and well tolerated in all NSCLC patients in this study. No serious adverse events (AEs) or discontinuations due to AEs were reported in the course of this research. Moreover, no

Table 1. Patient characteristics. CR, complete response; PR, partial response; SD, stable disease; PD, progressive disease; WT, wild type; AJCC, American Joint Committee on Cancer.

Characteristics	Total	EGFR exon 19 deletions	EGFR exon 21 point mutations	EGFR (WT)	Unknown
Patients, *n* (%)	75	17 (23%)	20 (27%)	33 (44%)	5 (6%)
Ages (years)					
Median	60	60	60	64	62
Range	45–80	47–80	45–78	45–78	45–80
Sex (male/female)	34:41	7:10	5:15	18:15	4:1
Smoking status					
Ever smoker	33	8	9	16	0
Never smoker	42	9	11	17	5
Stage (AJCC)					
I	10	7	1	2	0
II	3	1	0	2	0
III	30	5	9	13	3
IV	32	4	10	16	2
Histology					
Adenocarcinoma	66	17	20	24	5
Squamous cell carcinoma	9	0	0	9	0
^{18}F-MPG PET/CT					
$SUV_{max} \geq 2.23$	42	16	16	6	4
$SUV_{max} < 2.23$	33	1	4	27	1
TKI therapy response					
CR	2	0	2	0	0
PR	31	11	11	6	3
SD	11	2	2	7	0
PD	27	2	3	20	2

obvious changes in vital signs or clinical laboratory test results were detected after ^{18}F-MPG injection.

The highest organ dose (OD) values for ^{18}F-MPG were estimated in the gallbladder, thyroid, bladder, and pancreas. The effective dose of ^{18}F-MPG for humans was estimated to be 6.3 ± 2.27 μSv/MBq (table S8) and well within the range of what has been known for other ^{18}F-labeled diagnostic radiotracers such as 19.0 μSv/MBq for ^{18}F-FDG. Hence, the application of ^{18}F-MPG as new PET imaging agent in humans was considered to be safe.

^{18}F-MPG PET/CT study in NSCLC patients

The potential of using ^{18}F-MPG as a diagnostic tracer was examined in NSCLC patients (n = 75; Fig. 3 and Table 1). One hour after injection, ^{18}F-MPG successfully delineated EGFR-activating mutant tumors, showing visually appreciable higher contrast than EGFR wild-type tumors (Fig. 4). The EGFR mutation status was confirmed by histological and amplification refractory mutation system (ARMS) polymerase chain reaction (PCR) (Fig. 5). In two patients with EGFR-activating mutations (who did not receive EGFR-TKI treatment), ^{18}F-MPG PET/CT images showed high uptake not only in primary tumors but also in metastatic lesions (Fig. 4B). In comparison, although ^{18}F-FDG PET/CT showed high tumor uptake in all patient groups, with no apparent visual difference among patients carrying different EGFR mutation status (Fig. 4).

To further evaluate the feasibility of using ^{18}F-MPG PET for imaging EGFR mutations in lung cancer patients, we compared the biodistribution characteristics of ^{18}F-MPG and ^{18}F-FDG in every NSCLC patient enrolled in this study (fig. S7 and table S9). We assessed ^{18}F-MPG and ^{18}F-FDG uptake in the tumor, brain, lung, liver, gallbladder, spleen, kidney, intestine, muscle, pancreas, heart, and blood (exceptions for patients 59 and 67 for ^{18}F-FDG). Our results showed that ^{18}F-FDG had significantly higher uptake than ^{18}F-MPG in the most normal organs (fig. S7), including the brain ($P < 0.0001$), lung ($P < 0.01$), spleen ($P < 0.0001$), kidney ($P < 0.0001$), intestine ($P < 0.\ 01$), heart ($P < 0.0001$), and blood ($P < 0.\ 01$). It was noted that ^{18}F-MPG displayed higher uptake than ^{18}F-FDG in the gallbladder ($P < 0.0001$), liver ($P < 0.0001$), and muscle ($P < 0.\ 01$).

Association between ^{18}F-MPG uptake and EGFR mutation status

^{18}F-MPG accumulation in tumors and organs was further quantified by measuring the regions of interests (ROIs) thrice and then calculating the mean SUV_{max} (maximum standard uptake value) (tables S9 and S10). Considering patient groups 1 to 3 as independent categories,

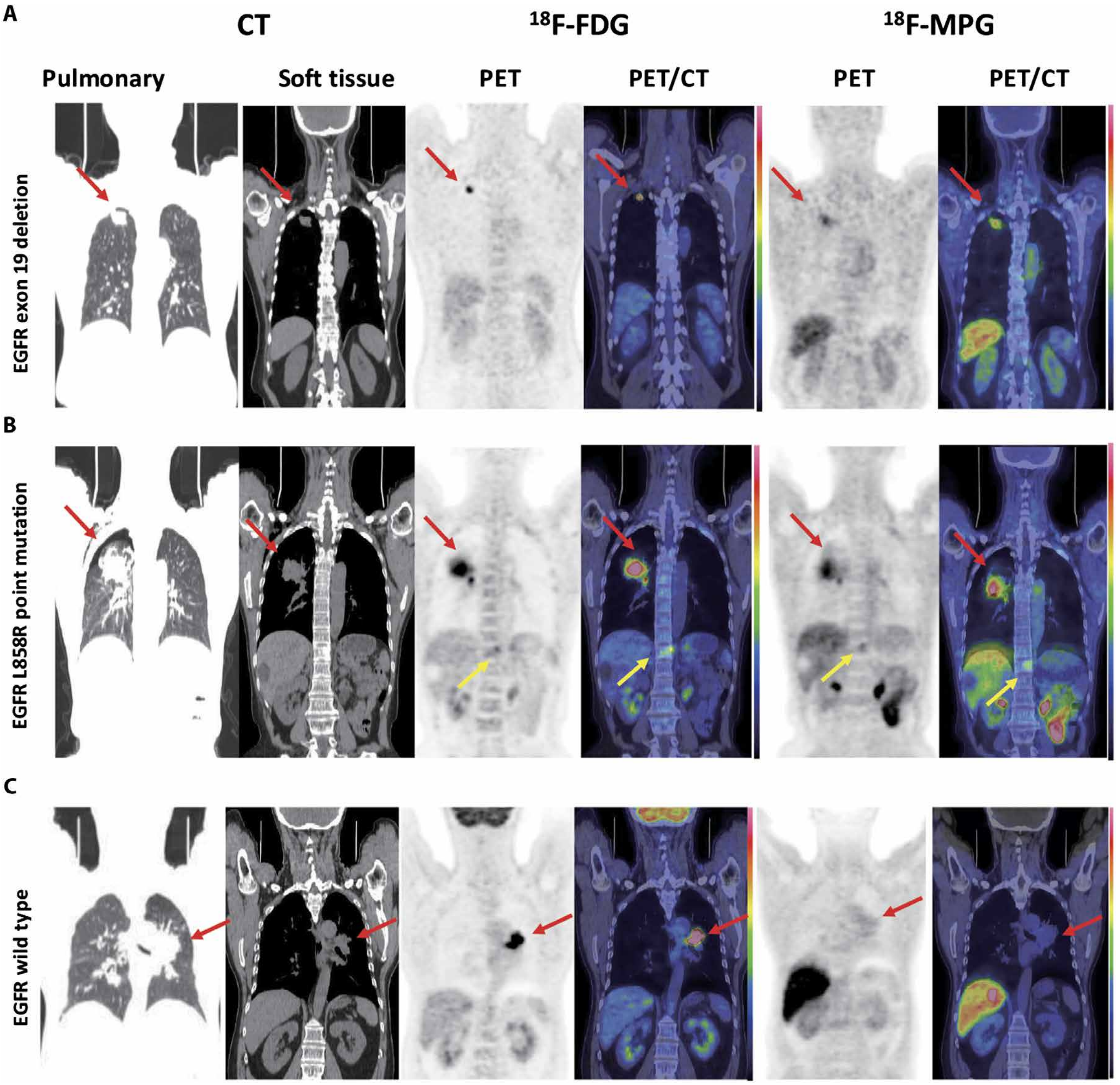

Fig. 4. Representative CT and PET/CT images of three patients with NSCLCs. (**A**) Patient (number 3) with an EGFR exon 19 E746-A750 deletion who did not receive EGFR-TKI treatment, with a tumor in the upper right lobe of the lung [red arrows; ^{18}F-MPG SUV$_{max}$ (maximum standard uptake value) of 3.93]. (**B**) Patient (number 36) with an EGFR exon 21 L858R point mutation, 15 days after gefitinib treatment. Tumor in the upper right lung lobe (red arrows; ^{18}F-MPG SUV$_{max}$ of 3.60) and spinal metastasis (yellow arrows; ^{18}F-MPG SUV$_{max}$ of 2.11) were observed both on ^{18}F-MPG and ^{18}F-FDG images. (**C**) Patient (number 54) with wild-type EGFR who did not receive EGFR-TKI treatment. Tumor in the left hilum (red arrows; ^{18}F-MPG SUV$_{max}$ of 1.38) was prominently observed on the ^{18}F-MPG image.

the analysis of variance (ANOVA) with the Newman-Keuls multiple comparison test confirmed that patients with EGFR-activating mutations had significantly higher ^{18}F-MPG mean SUV$_{max}$ than those with wild-type EGFR ($F_{2,\,67} = 16.30$, $P < 0.0001$; Fig. 6A). A small decrease in ^{18}F-MPG uptake was observed in patients with EGFR-activating mutations after EGFR-TKI treatment, but these differences did not reach statistical significance. The mean SUV$_{max}$ values for ^{18}F-FDG uptakes were significantly higher than ^{18}F-MPG in all groups (table S10); however, no associations were found between EGFR mutation status and ^{18}F-FDG uptake ($F_{2,\,65} = 0.3036$, $P = 0.7392$; Fig. 6B). Moreover, no association was found between ^{18}F-MPG uptake and EGFR exon 19 deletion or EGFR 21 point mutation ($P = 0.8486$; Fig. 6C).

The receiver operating characteristic (ROC) curve obtained from comparing EGFR mutation status with SUV$_{max}$ yielded an area under the curve (AUC) of 0.8440 [95% confidence interval (CI), 0.7476 to 0.9404; Fig. 6D]. When an SUV$_{max}$ of 2.23 was used to discriminate EGFR-activating mutant tumors (pre-TKIs and post-TKIs) and EGFR wild-type tumors, the sensitivity and specificity of the model were 86.49% (95% CI, 71.23 to 95.46%) and 81.82% (95% CI, 64.54 to 93.02%), respectively. A concordance of 84.29% was found between ^{18}F-MPG uptake and ARMS PCR.

^{18}F-MPG SUV$_{max}$ and survival

The median progression-free survival (PFS) of all patients was 225 days (95% CI, 146.5 to 202.1 days). Patients with EGFR-activating mutations had longer PFS than those carrying wild-type EGFR [hazard ratio (HR), 0.2135; 95% CI, 0.04517 to 0.2925; $P < 0.0001$; Fig. 6E]. PFS based on the study-specified ^{18}F-MPG SUV$_{max}$ cutoff of 2.23 is

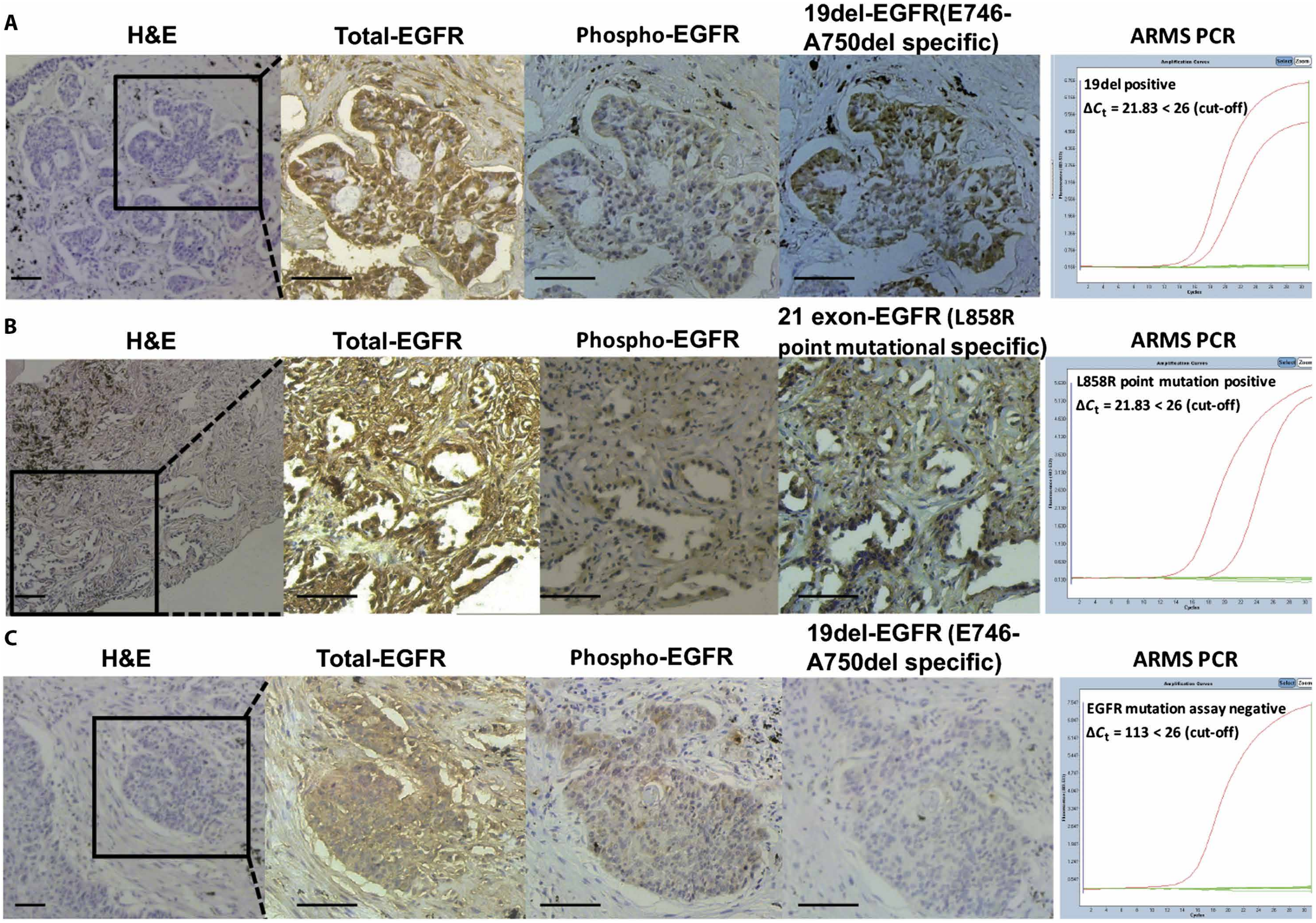

Fig. 5. EGFR mutation status of patients with NSCLC, detected by histological examination and ARMS PCR. (**A**) Histological and amplification refractory mutation system (ARMS) polymerase chain reaction (PCR) confirmation of a patient (number 3) with EGFR exon 19 deletion: hematoxylin and eosin (H&E) staining at ×10 magnification. Scale bar, 100 μm. Immunohistochemistry for total-EGFR, phosphorylated EGFR (phospho-EGFR), and E746-A750del–specific EGFR at ×20 magnification from inset in (B). Scale bars, 50 μm. ARMS PCR: $\Delta C_t = 18.57 < 26$ (cutoff). (**B**) Histological and ARMS PCR confirmation of a patient (number 36) with EGFR exon 21 L858R point mutation: H&E staining at ×10 magnification. Scale bar, 100 μm. Immunohistochemistry for total-EGFR, phospho-EGFR, and L858R-specific EGFR at ×20 magnification from inset in (B). Scale bars, 50 μm. ARMS PCR: $\Delta C_t = 21.83 < 26$ (cutoff). (**C**) Histological and ARMS PCR confirmation of a patient (number 54) with wild-type EGFR: H&E staining at ×10 magnification. Scale bar, 100 μm. Immunohistochemistry for total-EGFR, phospho-EGFR, and E746-A750 del–specific EGFR at ×20 magnification from inset in (C). Scale bars, 50 μm. ARMS PCR: $\Delta C_t = 113 > 26$ (cutoff).

shown in Fig. 6F. When using a cutoff of 2.23 for ^{18}F-MPG SUV$_{max}$, a significant association with PFS was observed (HR, 0.2083; 95% CI, 0.03406 to 0.2438; $P < 0.0001$). The median PFS of patients with ^{18}F-MPG SUV$_{max}$ ≥2.23 in this series was 348 days, whereas the median PFS of patients with ^{18}F-MPG SUV$_{max}$ <2.23 in this series was 183 days. These results clearly demonstrated that NSCLC patients with high ^{18}F-MPG SUV$_{max}$ benefited from EGFR-TKI treatment.

Correlation of ^{18}F-MPG PET/CT with response to therapy

Therapy response to EGFR-TKIs was assessed by CT imaging in 71 patients (Fig. 3 and Table 1) following standard response criteria: complete response (CR), partial response (PR), stable disease (SD), and progressive disease (PD). The 72.73% (24 of 33) of patients with EGFR-activating mutations (identified by ARMS PCR) demonstrated objective responses (CR or PR) to EGFR-TKIs. In contrast, in the unselected patient population, the response rate was only 45.45% (30 of 66). The total number of unselected patients was 66 because we could not obtain EGFR mutation status measurements (by ARMS PCR) in five patients. Of the 38 patients receiving EGFR-TKI therapy identified by ^{18}F-MPG PET/CT (^{18}F-MPG SUV$_{max}$ ≥2.23), 31 achieved objective responses (CR or PR), and 4 additional patients showed SD. Thus, ^{18}F-MPG PET/CT displayed detection sensitivity to EGFR-TKIs in 81.58% (31 of 38) of the selected patients. The objective response in unselected ^{18}F-MPG PET/CT imaging patients was 46.48% (33 of 71).

After EGFR-TKI therapy with gefitinib, one patient carrying EGFR exon 19 E746-A750del experienced disease stabilization during 20 months until tumor regression. Six months after receiving gefitinib, ^{18}F-MPG SUV$_{max}$ was 2.31, and after disease regression, it decreased to 2.01 (Fig. 7A). Further analysis of biopsied tissue revealed conversion from an EGFR-activating mutation phenotype to EGFR wild type (fig. S8).

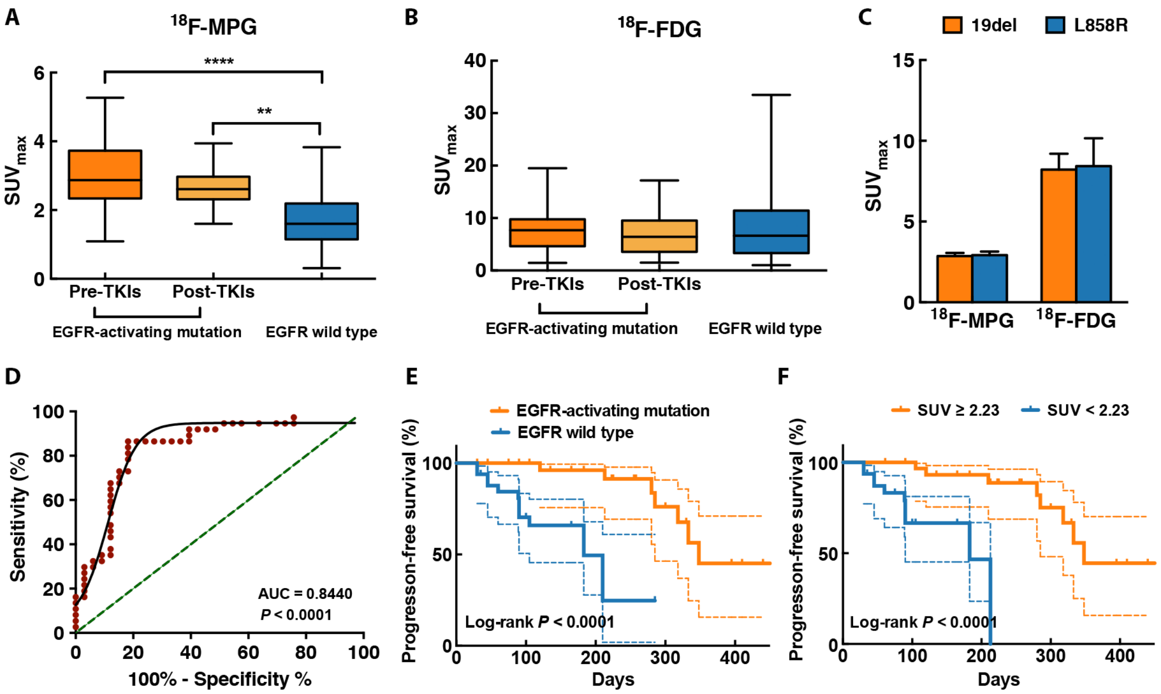

Fig. 6. Correlation between ^{18}F-MPG uptake and EGFR mutation status in patients with NSCLC and progression-free survival. (**A** and **B**) Box plot of ^{18}F-MPG SUV_{max} (A) and ^{18}F-FDG SUV_{max} (B) for patients with NSCLC with EGFR-activating mutation and wild-type EGFR, pre-TKI treatment and post-TKI treatment. Data are means ± SD. $^{**}P < 0.01$ and $^{****}P < 0.0001$, ANOVA with the Newman-Keuls multiple comparison test. (**C**) Box plot of ^{18}F-MPG SUV_{max} and ^{18}F-FDG SUV_{max} for patients with NSCLC with EGFR exon 19 deletion and EGFR exon 21 L858R point mutation. No association was found between ^{18}F-MPG uptake and EGFR exon 19 deletion or EGFR 21 point mutation. $P = 0.8486$, one-way ANOVA. (**D**) Receiver operating characteristic curve representing the sensitivity and specificity of ^{18}F-MPG SUV_{max} for predicting the presence of EGFR mutation status in patients with NSCLC [area under the curve (AUC) = 0.8440, $P < 0.0001$]. (**E**) Kaplan-Meier plots of progression-free survival according to EGFR mutation. HR (95% CI), 0.2135 (0.04517 to 0.2925); $P < 0.0001$. (**F**) Kaplan-Meier plots of progression-free survival according to ^{18}F-MPG SUV_{max}. HR (95% CI), 0.2083 (0.03406 to 0.2438); $P < 0.0001$.

The 81.82% (27 of 33) of patients with wild-type EGFR had ^{18}F-MPG SUV_{max} <2.23. Five of 33 patients with wild-type EGFR with ^{18}F-MPG SUV_{max} ≥2.23 all had therapy response or SD after treatment with EGFR-TKIs. The tumor EGFR mutation status was unknown in the remaining five patients. Of three patients whose tumors were ^{18}F-MPG SUV_{max} ≥2.23, two responded to EGFR-TKIs (Fig. 7B).

DISCUSSION

The precise quantification of EGFR mutation status in tumors allows for the accurate selection of patients for EGFR-TKI treatment while promoting the design of more effective therapeutic strategies. However, new biotechniques are needed to detect the intra- and intertumor EGFR mutation status in patients and thereby avoid unoptimized EGFR-TKI–based therapy. Noninvasive molecular imaging techniques using radiolabeled tracers for PET imaging have recently been developed to evaluate and quantify EGFR mutation status (*21*). Previously reported PET imaging tracers targeting EGFR at the kinase level include small molecules labeled with ^{11}C, ^{18}F, and ^{124}I-IPQA (*24*–*30*). Although two EGFR-targeting ^{11}C-labeled compounds (^{11}C-PD153035 and ^{11}C-erlotinib) have been assessed in patients, the short half-life of ^{11}C (20.38 min) limits its broader use in the clinic (*31*, *32*). Moreover, most of the aforementioned tracers are too lipophilic to be rapidly eliminated from the body. To solve these problems, considerable efforts have recently been invested into developing PEGylated anilinoquinazoline derivatives labeled with ^{18}F (half-life is 109.8 min) for imaging mutant EGFR kinases (*10*). However, to date, none of these ^{18}F-labeled TKIs has been used in clinical imaging of NSCLC patients. Here, we show that ^{18}F-MPG, a radiotracer targeting an EGFR-activating mutation, can be used to select NSCLC patients for EGFR-TKI therapy and to monitor treatment efficacy.

We have designed and synthesized ^{18}F-MPG on the basis of the structure of a quinazoline derivative. In this molecule, the PEG functional group is attached to the quinazoline ring at 7-position to increase hydrophilicity, and ^{18}F is attached at the end of the PEG4 chain. ^{18}F-MPG can then be easily prepared by a one-step radiosynthesis with good radiochemical yields, high purity, and highly specific activity. Our in vitro experiments in NSCLC cultured cells show that ^{18}F-MPG and QD620-MPG have significantly higher accumulation in EGFR E746-A750del cells when compared with EGFR L858R/T790M, EGFR-negative, or EGFR wild-type cells, and this preferential binding was confirmed in blocking assays with gefitinib, which competes for binding to the same site in the EGFR-activating mutant kinase domain. In addition, biochemical assays further indicate that F-MPG has increased inhibitory activity for EGFR E746-A750del cells when compared to EGFR L858R/T790M, EGFR-negative, or EGFR wild-type cells. Together, these data demonstrate that F-MPG activity is much higher for EGFR with activating mutations than for inactive mutant EGFR. Finally, molecular docking assays reveal that F-MPG adopts a similar conformation to PD153035 in the EGFR binding site, and key interactions between the quinazoline ring and EGFR residues remain, in agreement with the binding specificity of the ligand.

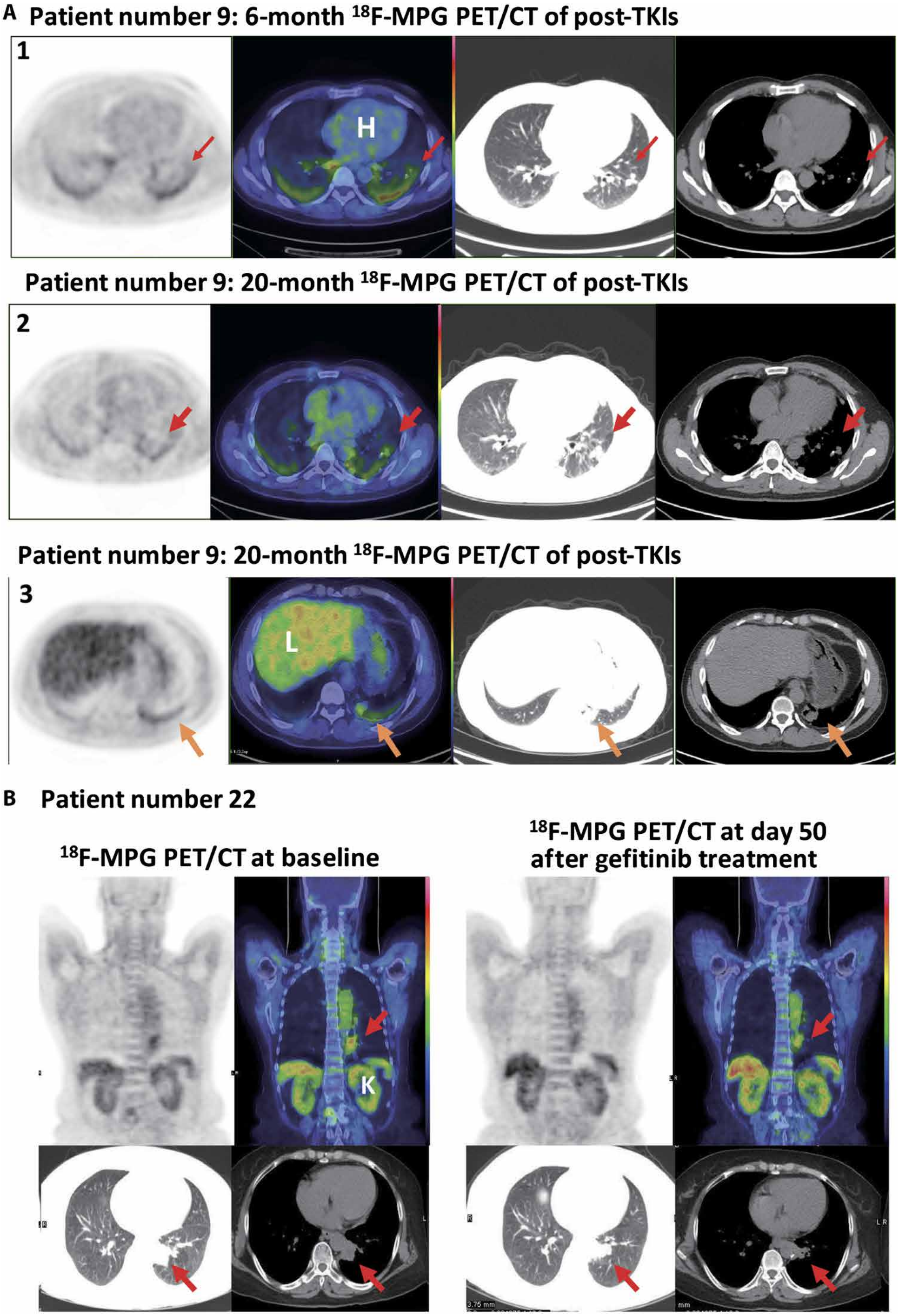
A Patient number 9: 6-month ^{18}F-MPG PET/CT of post-TKIs

Patient number 9: 20-month ^{18}F-MPG PET/CT of post-TKIs

Patient number 9: 20-month ^{18}F-MPG PET/CT of post-TKIs

B Patient number 22

^{18}F-MPG PET/CT at baseline

^{18}F-MPG PET/CT at day 50 after gefitinib treatment

Fig. 7. Examples of ^{18}F-MPG PET/CT imaging monitoring the change of EGFR mutation status and EGFR-TKI therapy response in patients with NSCLC. (**A**) Patient with NSCLC with a shift in tumor from EGFR-activating mutation to EGFR wild type. Scans from a 47-year-old Asian male (number 9) with smoking history and lung adenocarcinoma are shown. Row 1: ^{18}F-MPG PET/CT tumor SUV$_{max}$ is 2.31 (red arrow), and EGFR gene test shows EGFR exon 19 E746-A750 deletion at 6 months after gefitinib treatment. Row 2: ^{18}F-MPG PET/CT tumor SUV$_{max}$ decreased to 2.01 (red arrow), and EGFR gene test with second fine-needle aspiration shows EGFR wild type at 20 months after gefitinib treatment. Row 3: 20 months after TKI ^{18}F-MPG PET/CT also showed that a new tumor appeared in the inferior lobe (orange arrow) indicating progressive disease. H, heart; L, liver. (**B**) From a patient with NSCLC with unknown EGFR mutation status, an example of ^{18}F-MPG PET/CT response: Scans from a 60-year-old Asian female (number 22) with no smoking history and lung adenocarcinoma are shown. Baseline ^{18}F-MPG PET/CT tumor SUV$_{max}$ is 3.04, and tumor size is 3.1 × 2.6 cm^2 (red arrow). ^{18}F-MPG PET/CT tumor SUV$_{max}$ has decreased to 2.61 at 50 days after gefitinib treatment, and the tumor was shrunk [tumor size, 2.3 × 1.3 cm^2 (red arrow)]. Marked ^{18}F-MPG response was seen on day 50, and PET/CT scan showed partial response. K, kidney.

PET imaging with ^{18}F-MPG in human NSCLC xenograft mouse models shows high imaging contrast and tracer specificity for EGFR-activating mutant tumors. Moreover, a much lower accumulation of ^{18}F-MPG in tumors with inactive EGFR mutation suggests that ^{18}F-MPG may differentiate tumors sensitive or resistant to EGFR-TKIs, and this is supported by the biodistribution data. Collectively, our in vitro assays and preclinical results show that EGFR mutation status can be noninvasively and repeatedly determined by ^{18}F-MPG.

A combination of high ^{18}F-MPG tumor uptake and low normal lung background allowed us to distinguish tumors with EGFR-activating mutations from EGFR wild-type tumors in clinical PET/CT studies in patients with NSCLC, as demonstrated by PET/CT image quantification analysis and by ANOVA and post hoc comparisons. Moreover, we show that NSCLC patients treated with gefitinib, erlotinib, or icotinib have a slight decrease in ^{18}F-MPG tumor accumulation. Nevertheless, ^{18}F-MPG SUV$_{max}$ is still higher than in EGFR wild-type tumors, in agreement with the preclinical data. These results suggest that ^{18}F-MPG PET/CT imaging may reveal residual EGFR-activating tumor sites after treatment with EGFR-TKIs. This information could provide useful for redesigning EGFR-TKI treatments; for instance, it may justify preceding the therapy with a more complex protocol. Thus, ^{18}F-MPG PET/CT imaging adds new valuable functional information on NSCLC patient response to EGFR-TKIs, which cannot be provided by traditional in vitro methods. The decrease in ^{18}F-MPG tumor accumulation is also observed in animal PET imaging but is more obvious than clinical study. In blocking assays, there is a twofold decrease in ^{18}F-MPG accumulation in HCC827 tumors in gefitinib pretreatment xenograft mice. The differences in ^{18}F-MPG uptake after EGFR-TKI treatment in the preclinical and clinical studies can be explained by differences in the gefitinib dose administered. We pretreated the HCC827 xenograft mice with excessive amounts of gefitinib (100 mg/kg) to occupy all the EGFR-activating tumor sites. However, high doses of gefitinib cause significant side effects in patients (dose-dependent and reversible diarrhea and acneiform rashes), and hence, the maximum dose of gefitinib used in the clinical treatments (750 mg/day per patient; average, 60 kg) was much lower than that used in preclinical blocking assays. Thus, in clinical patients, there were still some residual EGFR-activating tumor sites available for ^{18}F-MPG binding after treatment with gefitinib, which explains the small decrease in ^{18}F-MPG accumulation detected in patients with EGFR-activating mutations after EGFR-TKI therapy.

ROC curves and AUCs calculated for ^{18}F-MPG SUV$_{max}$ measurements validate a cutoff value of SUV$_{max}$ ≥2.23 for predicting EGFR-activating mutation status in NSCLC patients. With SUV$_{max}$ ≥2.23, the sensitivity, specificity, and predictive accuracy of ^{18}F-MPG PET can reach 86.49, 81.82, and 84.29%, respectively. Notably, because ^{18}F-MPG SUV$_{max}$ is closely associated with PFS, ^{18}F-MPG PET/CT imaging can identify patients responsive to EGFR-TKI sensitivity (this subpopulation could be considered for EGFR-TKI treatment). The objective response rate in patients with ^{18}F-MPG SUV$_{max}$ ≥2.23 was about two times higher than that in unselected patients, and those patients had good outcomes after EGFR-TKI therapy. However, this cutoff value should be considered as exploratory because our study only includes a moderate number of patients.

^{18}F-FDG is the most widely used PET tracer for tumor imaging. Thus, it is important to compare the performance of ^{18}F-MPG and ^{18}F-FDG when imaging EGFR-activating mutations in patients with NSCLC to fully assess the clinical translational potential of the new tracer. ^{18}F-FDG shows significantly higher uptake in normal organs than ^{18}F-MPG, including the brain, lung, spleen, kidney, intestine, heart, and blood, further suggesting that ^{18}F-MPG has excellent clinical translational potential. Moreover, low ^{18}F-MPG uptake in the normal brain allows the easy detection of EGFR-activating metastasis, another advantage of this tracer, when compared to ^{18}F-FDG. We also found no correlation between ^{18}F-FDG tumor uptake and EGFR mutation status or response to EGFR-TKI treatment, whereas previous studies searching for such an association had reached conflicting conclusions (*33*, *34*). On the other hand, ^{18}F-MPG shows specificity for EGFR-activating mutant tumors, including primary tumor and metastases. Early PET/CT imaging with ^{18}F-MPG may predict patient response to EGFR-TKI treatment.

Despite these promising results, some questions still need to be addressed for the optimal translation of ^{18}F-MPG into the clinic. First, our patient study was performed retrospectively, possibly leading to potential bias. Second, a multicenter clinical trial study with a larger patient sample size is also required. Third, although the PEG functional group increases the water solubility of ^{18}F-MPG, the tracer still shows relatively higher uptake than ^{18}F-FDG in the liver and gallbladder, which could prevent diagnosis of metastases in these organs. In the future, ^{18}F-MPG should be optimized to increase water solubility and decrease lipid solubility. Finally, optimal dosing, imaging time, and parameters for ^{18}F-MPG PET/CT imaging need to be investigated. Whether other factors, such as dosage or type of EGFR-TKIs, might affect ^{18}F-MPG uptake should also be considered.

In summary, our results demonstrate that ^{18}F-MPG uptake is significantly increased in NSCLC tumors harboring EGFR-activating mutations, based on analysis of the association between EGFR mutation status and ^{18}F-labeled small molecular TKI uptake in NSCLC patients. When compared to analyses in tumor tissues and plasma samples for detecting genetic alterations, ^{18}F-MPG PET/CT quantitatively detected EGFR-activating mutation tumors (primary or metastatic) and displayed the position and morphology of the NSCLCs directly. Thus, ^{18}F-MPG PET/CT imaging is a promising method for the noninvasive identification of patients with NSCLC who may benefit from EGFR-TKI therapy and for predicting and monitoring EGFR-TKI treatment outcome.

MATERIALS AND METHODS

Study design

The goal of this study was to assess ^{18}F-MPG as a PET/CT tracer for monitoring EGFR-activating mutation status and identifying NSCLC patients responsive to EGFR-TKI treatment. We tested the selective binding and uptake properties of ^{18}F-MPG and QD620-MPG to EGFR-activating mutation kinase in vitro and in vivo. Then, we demonstrated the efficacy of ^{18}F-MPG PET in identifying NSCLC tumors sensitive to EGFR-TKIs in mice. We also evaluated the feasibility of using ^{18}F-MPG PET/CT imaging in adult patients with NSCLC with different EGFR mutation status (primary and metastatic tumors) in a clinical trial (ClinicalTrials.gov: NCT02717221).

Preparation of ^{18}F-MPG

The synthesis of the T-MPG precursor was described in Supplementary Materials and Methods (fig. S1). For the one-step ^{18}F labeling, the solution of ^{18}F-fluoride (K_2CO_3/Kryptofix 222) was azeotropically dried in two steps by a GE TRACERlab FX-FN synthesizer. Next, T-MPG dissolved in 0.4 ml of dimethyl sulfoxide was added into the dried ^{18}F-fluoride and then heated at 120°C for 10 min in the presence of helium. After cooling to 35°C, the mixture in the reaction vessel was purified in an HPLC (high-performance liquid chromatography) column (VP 250/16 NUCLEOSIL 100-7 C18, MN) by using the eluent (ethanol/water, 50:50; 8 ml/min). To determine the radiochemical purity of ^{18}F-MPG, radio thin-layer chromatography was performed by silica gel plate and acetonitrile (95%). To measure the specific activity of ^{18}F-MPG, we first established a standard curve with F-MPG by injecting five different quantities of F-MPG into HPLC (Alltech Series 1500), and then the activity of ^{18}F-MPG in 0.1 ml was measured with a radioactivity meter before injection into the HPLC. On the basis of the linear standard curve, we measured the mass of ^{18}F-MPG and defined the specific activity of ^{18}F-MPG: SA = A/m, where SA means specific activity, A is the amount of radioactivity of ^{18}F-MPG loaded into HPLC (corrected by the time elapsed since the amount of radioactivity was measured), and *m* is the mass of ^{18}F-MPG (based on the F-MPG standard curve).

In vitro cell uptake study

The cell uptake and blocking assays were performed as previously described (*35*). Briefly, HCC827, H1975, H520, and H358 cells were seeded into 12-well plates at a density of 1 × 10^5 per well and incubated with ^{18}F-MPG [37 kilobecquerel (kBq)/1.0 ml per well] at 37°C for 15, 30, 60, and 120 min. After washing three times with cold phosphate-buffered saline, the cells were harvested in 200 μl of 0.1 N NaOH (EMD Millipore Corporation). Suspensions of HCC827, H1975, H520, and H358 cells were collected individually and measured in a γ-counter (2480, PerkinElmer). Cell uptake was expressed as a percentage of the decay-corrected total input radioactivity. For blocking studies, gefitinib (100 μM) was added to the HCC827 cells. After 1-hour incubation, the HCC827 cell uptake assay was repeated as described above. The cell uptake and blocking studies were conducted three times with triplicate wells. Data are expressed as the percent added dose after decay correction.

In vivo PET of mice and biodistribution

PET scans and image analyses were performed with a clinical time-of-flight (TOF) 64-slice PET/CT scanner (Discovery 790 Elite; GE Healthcare). Each HCC827, H1975, H520, or H358 tumor-bearing mouse was injected via the tail vein with ^{18}F-MPG with 3.7 MBq (100 μCi; 0.1 nmol in 100 μl) or ^{18}F-FDG with 7.4 MBq (200 mCi) under isoflurane anesthesia ($n = 6$ per group). ^{18}F-MPG PET was acquired for 3 min in two-dimensional (2D) mode at 30 min, 1 hour, and 2 hours after injection. ^{18}F-FDG PET was acquired for 3 min in 2D mode at 1 hour after injection. The PET images were reconstructed on a 512 × 512 matrix for a 15-cm-diameter field of view by ordered subsets expectation maximization (OSEM) algorithm. The PET, CT, and fused images were visualized with the Advantage Workstation version AW4.6 software package (GE Healthcare). For blocking experiments with HCC827 tumor-bearing mice, gefitinib (100 mg/kg) was injected into xenograft-bearing nude mice ($n = 5$ per group) before PET imaging. After 1 hour, all the mice underwent imaging processing as described above. For each PET scan, ROIs were drawn over the tumor and normal tissue using the Advantage Workstation version AW4.6 software (GE Healthcare) on decay-corrected whole-body coronal images. The maximum radioactivity counts within a tumor or a normal tissue were obtained from mean pixel values within the multiple ROI volumes and then converted to megabecquerels per milliliter using a conversion factor. These values were then used to calculate an image ROI-derived % ID/g, as we previously described (*35*).

For the ex vivo biodistribution experiments, female athymic nude mice bearing HCC827, H1975, H520, or H358 xenografts were injected with 0.925 MBq (25 μCi; 100 pmol in 200 μl) of ^{18}F-MPG through the tail vein to evaluate the distribution of the tracer in the tumor tissues and major organs. At 30 min, 1 hour, and 2 hours after injection of the tracer, the tumor-bearing mice were sacrificed and dissected ($n = 6$ per group). Tumors and major organs were collected and wet-weighed. The radioactivity in the wet whole tissue was measured with a γ-counter (2480, PerkinElmer). The results were expressed as % ID/g.

Patient characteristics

Patients were recruited from The Fourth Hospital of Harbin Medical University between December 2014 and May 2017. Seventy-five of 102 patients with local NSCLC were considered eligible for the study. Biopsies of the primary tumors or metastatic lesions were obtained to diagnose NSCLC and determine EGFR mutation status by genetic testing in some of the patients (Fig. 3 and Table 1). When an excisional biopsy was performed, fresh or freshly frozen tumor was submitted to Shanghai ACKERMAN Pathology and Diagnostics Company (Shanghai, China) for quantitative measurement of EGFR mutation status by using the ARMS PCR method or gene sequencing. Other entry criteria included an age of 18 years or older, a life expectancy of at least 12 weeks, the presence of a malignant lesion within the chest of at least 0.5 cm in diameter as measured by CT, and written informed consent. Exclusion criteria were claustrophobia, pregnancy, lactation, and metal implants in the thorax. This study was approved by the Medical Ethics Review Committee of The Fourth Hospital of Harbin Medical University and was registered at ClinicalTrials.gov.

To evaluate the suitability of using ^{18}F-MPG imaging to select NSCLC patients sensitive to EGFR-TKI treatment, we analyzed 75 patients with histologically proven, local NSCLC with or without metastases. EGFR mutation status was confirmed quantitatively by ARMS PCR or gene sequencing in 70 patients. EGFR mutation status could not be determined in five patients because of inadequate tissue samples.

Baseline characteristics of all patients are shown in Table 1 and Fig. 3. The patients were divided into four groups as follows: group 1, patients with EGFR-activating mutations in tumors who did not receive any treatment before the study (24 patients); group 2, patients with EGFR-activating mutations in tumors who received EGFR-TKIs during this study (13 patients); group 3, patients with wild-type EGFR in tumors who did not receive any treatment before this study (33 patients); and group 4, patients without the EGFR mutation status measurement results who did not receive any treatments (5 patients).

PET/CT imaging studies in patients

The ^{18}F-MPG and ^{18}F-FDG studies used PET/CT scanning (Discovery 790 Elite; GE Healthcare) and were conducted on two separate days. All patients participated in the ^{18}F-MPG study, whereas only 73 of 75 patients participated in both ^{18}F-MPG and ^{18}F-FDG studies. About 259 MBq (7 mCi) of ^{18}F-MPG was administered intravenously within 5 min. Scanning was initiated 1 hour after administration of the tracer. The ^{18}F-FDG PET scans (3.7 MBq/kg body weight) were acquired after the patients fasted for at least 6 hours, and the blood glucose was <180 mg/dl. The images were evaluated qualitatively by three experienced nuclear medicine physicians independently. The SUV_{max} normalized to body weight (kBq/ml) was calculated within the ROI.

Whole-body CT scans were acquired for attenuation correction by using a low-dose protocol (40 mA, 120 keV, a 512 × 512 matrix, 3.75-mm slice thickness, increment of 30 mm/s, rotation time of 0.5 s, and pitch index of 0.8). Subsequently, PET data were acquired in 3D mode with a 200 × 200 matrix with 3-min imaging time per bed position. After decay and scatter correction, the data were reconstructed (Advantage Workstation version AW4.6, 3D-OSEM, VUE Point FX–TOF correction, Sharp-IR). To quantify tracer accumulation, a volume of interest using a 3D sphere was placed over the primary lung tumor, lymph nodes, and distant metastases avoiding necrosis, blood vessels, and normal lung tissue as much as possible on a workstation (Advantage Workstation 4.6; GE Healthcare).

Safety assessment

Patient safety was assessed and graded according to the Common Terminology Criteria for Adverse Events (version 4.03) (*36*) by measuring the blood pressure, respiratory rate, pulse rate, temperature, and routine blood and urine tests. Within the first 24 hours after ^{18}F-MPG injection, the research team kept phone contact with each subject monitoring for potential AE responses. We noted and analyzed any possible side effects during and within 1 week after ^{18}F-MPG PET/CT scan.

Statistical analysis

To assess the association between ^{18}F-MPG or ^{18}F-FDG uptake and EGFR mutation status, we performed statistical analyses in two ways: (i) Student's t test was used to compare quantitative data between two independent samples; and (ii) for comparisons involving more than two categories, one-way ANOVA, followed by the Newman-Keuls post hoc test, was performed (GraphPad Prism 5). ANOVA F ratio df were listed as $F_{x,y}$ in the text and legends for the nominator (x) and denominator (y). An ROC curve was computed for $\mathrm{SUV_{max}}$, thereby evaluating the ability to discriminate EGFR-activating mutation status and identifying the optimum ^{18}F-MPG PET/CT $\mathrm{SUV_{max}}$ cutoff value. The criteria for determining the optimal cutoff value was the $\mathrm{SUV_{max}}$ point on the curve with the minimum distance from the upper left corner of the unit square and the point where the Youden's index (sensitivity + specificity − 1) was maximal. The total AUC and its 95% CI were calculated. The sensitivity, specificity, and diagnostic accuracy were calculated as indicators of its accurateness in the prediction of EGFR-activating mutations. PFS estimates were calculated according to the Kaplan-Meier method. Statistical significance was set at $P < 0.05$. Quantitative values were expressed as means ± SD or SEM as indicated. Statistical analysis was performed with IBM SPSS Statistics v. 22.0.

SUPPLEMENTARY MATERIALS

www.sciencetranslationalmedicine.org/cgi/content/full/10/431/eaan8840/DC1
Materials and Methods
Fig. S1. Synthetic scheme of T-MPG (compound 9) and F-MPG (compound 13).
Fig. S2. Radioactivity chromatograms of ^{18}F-MPG.
Fig. S3. Characterization of HCC827, H1975, H520, and H358 cell lines and xenograft tumor models in vitro and ex vivo.
Fig. S4. Predicted binding modes of F-MPG and PD153035 with the EGFR wild type, EGFR exon 19 E746-A750 deletion homology model, and EGFR L858R/T790M double mutant.
Fig. S5. Uptake of MPG analogs in NSCLC cells.
Fig. S6. Accumulation of ^{18}F-MPG in different mice tumor xenografts.
Fig. S7. Biodistribution of ^{18}F-MPG and ^{18}F-FDG in all patients with NSCLC at 60 min after injection.
Fig. S8. Gene sequencing confirmation of an NSCLC patient (number 9) with a shift in tumor from EGFR-activating mutation to EGFR wild type.
Table S1. Quantitative ^{18}F-MPG PET ROI analysis of organ uptake in different tumor xenografts in mice at 30 min (n = 6 per group).
Table S2. Quantitative ^{18}F-MPG PET ROI analysis of organ uptake in different tumor xenografts in mice at 1 hour (n = 6 per group).
Table S3. Quantitative ^{18}F-MPG PET ROI analysis of organ uptake in different tumor xenografts in mice at 2 hours (n = 6 per group).
Table S4. Quantitative ^{18}F-FDG PET ROI analysis of organ uptake in different tumor xenografts in mice at 1 hour (n = 6 per group).
Table S5. Biodistribution of ^{18}F-MPG in different tumor xenografts in mice at 30 min (n = 6 per group).
Table S6. Biodistribution of ^{18}F-MPG in different tumor xenografts in mice at 1 hour (n = 6 per group).
Table S7. Biodistribution of ^{18}F-MPG in different tumor xenografts in mice at 2 hours (n = 6 per group).
Table S8. First-in-human data, OD in microsievert/megabecquerel.
Table S9. ^{18}F-MPG and ^{18}F-FDG $\mathrm{SUV_{max}}$ in all NSCLC patient organs 60 min after injection.
Table S10. Tumor accumulation of ^{18}F-MPG and ^{18}F-FDG in different groups of NSCLC patients at 60 min.

REFERENCES AND NOTES

1. "Precision Medicine" Lister Hill National Center for Biomedical Communications, U.S. National Library of Medicine, National Institutes of Health, Department of Health & Human Services, published online 1 December 2016; https://ghr.nlm.nih.gov/primer/precisionmedicine/definition.
2. Moving toward precision medicine. *Lancet* **378**, 1678 (2011).
3. B. Pasche, S. C. Grant, Non-small cell lung cancer and precision medicine: A model for the incorporation of genomic features into clinical trial design. *JAMA* **311**, 1975–1976 (2014).
4. J. G. Paez, P. A. Jänne, J. C. Lee, S. Tracy, H. Greulich, S. Gabriel, P. Herman, F. J. Kaye, N. Lindeman, T. J. Boggon, K. Naoki, H. Sasaki, Y. Fujii, M. J. Eck, W. R. Sellers, B. E. Johnson, M. Meyerson, EGFR mutations in lung cancer: Correlation with clinical response to gefitinib therapy. *Science* **304**, 1497–1500 (2004).
5. T. J. Lynch, D. W. Bell, R. Sordella, S. Gurubhagavatula, R. A. Okimoto, B. W. Brannigan, P. L. Harris, S. M. Haserlat, J. G. Supko, F. G. Haluska, D. N. Louis, D. C. Christiani, J. Settleman, D. A. Haber, Activating mutations in the epidermal growth factor receptor underlying responsiveness of non–small-cell lung cancer to gefitinib. *N. Engl. J. Med.* **350**, 2129–2139 (2004).
6. R. Rosell, E. Carcereny, R. Gervais, A. Vergnenegre, B. Massuti, E. Felip, R. Palmero, R. Garcia-Gomez, C. Pallares, J. M. Sanchez, R. Porta, M. Cobo, P. Garrido, F. Longo, T. Moran, A. Insa, F. De Marinis, R. Corre, I. Bover, A. Illiano, E. Dansin, J. de Castro, M. Milella, N. Reguart, G. Altavilla, U. Jimenez, M. Provencio, M. A. Moreno, J. Terrasa, J. Muñoz-Langa, J. Valdivia, D. Isla, M. Domine, O. Molinier, J. Mazieres, N. Baize, R. Garcia-Campelo, G. Robinet, D. Rodriguez-Abreu, G. Lopez-Vivanco, V. Gebbia, L. Ferrera-Delgado, P. Bombaron, R. Bernabe, A. Bearz, A. Artal, E. Cortesi, C. Rolfo, M. Sanchez-Ronco, A. Drozdowskyj, C. Queralt, I. de Aguirre, J. L. Ramirez, J. J. Sanchez, M. A. Molina, M. Taron, L. Paz-Ares; Istituto Europeo di Oncologia; Istituto Regina Elena; Centro di Riferimento Oncologico, Erlotinib versus standard chemotherapy as first-line treatment for European patients with advanced EGFR mutation-positive non-small-cell lung cancer (EURTAC): A multicentre, open-label, randomised phase 3 trial. *Lancet Oncol.* **13**, 239–246 (2012).
7. T. S. Mok, Y.-L. Wu, S. Thongprasert, C.-H. Yang, D.-T. Chu, N. Saijo, P. Sunpaweravong, B. Han, B. Margono, Y. Ichinose, Y. Nishiwaki, Y. Ohe, J.-J. Yang, B. Chewaskulyong, H. Jiang, E. L. Duffield, C. L. Watkins, A. A. Armour, M. Fukuoka, Gefitinib or carboplatin–paclitaxel in pulmonary adenocarcinoma. *N. Engl. J. Med.* **361**, 947–957 (2009).
8. J. H. Schiller, D. Harrington, C. P. Belani, C. Langer, A. Sandler, J. Krook, J. Zhu, D. H. Johnson; Eastern Cooperative Oncology Group, Comparison of four chemotherapy regimens for advanced non–small-cell lung cancer. *N. Engl. J. Med.* **346**, 92–98 (2002).
9. M. Ratti, G. Tomasello, Emerging combination therapies to overcome resistance in EGFR-driven tumors. *Anticancer Drugs* **25**, 127–139 (2014).
10. H. H. Yeh, K. Ogawa, J. Balatoni, U. Mukhapadhyay, A. Pal, C. Gonzalez-Lepera, A. Shavrin, S. Soghomonyan, L. Flores II, D. Young, A. Y. Volgin, A. M. Najjar, V. Krasnykh, W. Tong, M. M. Alauddin, J. G. Gelovani, Molecular imaging of active mutant L858R EGF receptor (EGFR) kinase-expressing nonsmall cell lung carcinomas using PET/CT. *Proc. Natl. Acad. Sci. U.S.A.* **108**, 1603–1608 (2011).
11. N. Xia, J. An, Q.-q. Jiang, M. Li, J. Tan, C.-p. Hu, Analysis of *EGFR*, *EML4-ALK*, *KRAS*, and *c-MET* mutations in Chinese lung adenocarcinoma patients. *Exp. Lung Res.* **39**, 328–335 (2013).
12. W. Brugger, N. Triller, M. Blasinska-Morawiec, S. Curescu, R. Sakalauskas, G. M. Manikhas, J. Mazieres, R. Whittom, C. Ward, K. Mayne, K. Trunzer, F. Cappuzzo, Prospective molecular marker analyses of *EGFR* and *KRAS* from a randomized, placebo-controlled study of erlotinib maintenance therapy in advanced non–small-cell lung cancer. *J. Clin. Oncol.* **29**, 4113–4120 (2011).
13. P. Pfeiffer, E. Nexø, S. M. Bentzen, P. P. Clausen, K. Andersen, C. Rose, Enzyme-linked immunosorbent assay of epidermal growth factor receptor in lung cancer: Comparisons with immunohistochemistry, clinicopathological features and prognosis. *Br. J. Cancer* **78**, 96–99 (1998).
14. J. Neumann, L. Wehweck, S. Maatz, J. Engel, T. Kirchner, A. Jung, Alterations in the EGFR pathway coincide in colorectal cancer and impact on prognosis. *Virchows Arch.* **463**, 509–523 (2013).
15. D. Shibata, Heterogeneity and tumor history. *Science* **336**, 304–305 (2012).
16. C. Swanton, Intratumor heterogeneity: Evolution through space and time. *Cancer Res.* **72**, 4875–4882 (2012).
17. R. Weissleder, U. Mahmood, Molecular imaging. *Radiology* **219**, 316–333 (2001).
18. R. Weissleder, Molecular imaging: Exploring the next frontier. *Radiology* **212**, 609–614 (1999).
19. H. C. Manning, World Molecular Imaging Congress 2015: Precision medicine visualized. *Mol. Imaging Biol.* **17**, 295–296 (2015).
20. J. M. Hoffman, S. S. Gambhir, Molecular imaging: The vision and opportunity for radiology in the future. *Radiology* **244**, 39–47 (2007).
21. S. S. Gambhir, Molecular imaging of cancer with positron emission tomography. *Nat. Rev. Cancer* **2**, 683–693 (2002).
22. M. Bos, J. Mendelsohn, Y. M. Kim, J. Albanell, D. W. Fry, J. Baselga, PD153035, a tyrosine kinase inhibitor, prevents epidermal growth factor receptor activation and inhibits growth of cancer cells in a receptor number-dependent manner. *Clin. Cancer Res.* **3**, 2099–2106 (1997).

23. J.-F. Goossens, E. Bouey-Bencteux, R. Houssin, J.-P. Hénichart, P. Colson, C. Houssier, W. Laine, B. Baldeyrou, C. Bailly, DNA interaction of the tyrosine protein kinase inhibitor PD153035 and its *N*-methyl analogue. *Biochemistry* **40**, 4663–4671 (2001).
24. X. Meng, B. W. Loo Jr., L. Ma, J. D. Murphy, X. Sun, J. Yu, Molecular imaging with ^{11}C-PD153035 PET/CT predicts survival in non–small cell lung cancer treated with EGFR-TKI: A pilot study. *J. Nucl. Med.* **52**, 1573–1579 (2011).
25. G. Abourbeh, B. Itamar, O. Salnikov, S. Beltsov, E. Mishani, Identifying erlotinib-sensitive non-small cell lung carcinoma tumors in mice using [^{11}C]erlotinib PET. *EJNMMI Res.* **5**, 4 (2015).
26. M.-R. Zhang, K. Kumata, A. Hatori, N. Takai, J. Toyohara, T. Yamasaki, K. Yanamoto, J. Yui, K. Kawamura, S. Koike, K. Ando, K. Suzuki, [^{11}C]gefitinib ([^{11}C]Iressa): Radiosynthesis, in vitro uptake, and in vivo imaging of intact murine fibrosarcoma. *Mol. Imaging Biol.* **12**, 181–191 (2010).
27. G. Ortu, I. Ben-David, Y. Rozen, N. M. T. Freedman, R. Chisin, A. Levitzki, E. Mishani, Labeled EGFr-TK irreversible inhibitor (ML03): In vitro and in vivo properties, potential as PET biomarker for cancer and feasibility as anticancer drug. *Int. J. Cancer* **101**, 360–370 (2002).
28. H. Su, Y. Seimbille, G. Z. Ferl, C. Bodenstein, B. Fueger, K. J. Kim, Y.-T. Hsu, S. M. Dubinett, M. E. Phelps, J. Czernin, W. A. Weber, Evaluation of [^{18}F]gefitinib as a molecular imaging probe for the assessment of the epidermal growth factor receptor status in malignant tumors. *Eur. J. Nucl. Med. Mol. Imaging* **35**, 1089–1099 (2008).
29. P. Slobbe, A. D. Windhorst, M. Stigter-van Walsum, E. F. Smit, H. G. Niessen, F. Solca, G. Stehle, G. A. M. S. van Dongen, A. J. Poot, A comparative PET imaging study with the reversible and irreversible EGFR tyrosine kinase inhibitors [^{11}C]erlotinib and [^{18}F]afatinib in lung cancer-bearing mice. *EJNMMI Res.* **5**, 14 (2015).
30. S. H.-H. Yeh, C.-F. Lin, F.-L. Kong, H.-E. Wang, Y.-J. Hsieh, J. G. Gelovani, R.-S. Liu, Molecular imaging of nonsmall cell lung carcinomas expressing active mutant EGFR kinase using PET with [^{124}I]-morpholino-IPQA. *Biomed. Res. Int.* **2013**, 549359 (2013).
31. J. Sun, L. Cai, K. Zhang, A. Zhang, P. Pu, W. Yang, S. Gao, A pilot study on EGFR-targeted molecular imaging of PET/CT with 11C-PD153035 in human gliomas. *Clin. Nucl. Med.* **39**, e20–e26 (2014).
32. I. Bahce, E. F. Smit, M. Lubberink, A. A. M. van der Veldt, M. Yaqub, A. D. Windhorst, R. C. Schuit, E. Thunnissen, D. A. M. Heideman, P. E. Postmus, A. A. Lammertsma, N. H. Hendrikse, Development of [^{11}C]erlotinib positron emission tomography for in vivo evaluation of EGF receptor mutational status. *Clin. Cancer Res.* **19**, 183–193 (2013).
33. C. Caicedo, M. J. Garcia-Velloso, M. D. Lozano, T. Labiano, C. Vigil Diaz, J. M. Lopez-Picazo, A. Gurpide, J. J. Zulueta, J. A. Richter Echevarria, J. L. Perez Gracia, Role of [^{18}F]FDG PET in prediction of *KRAS* and *EGFR* mutation status in patients with advanced non-small-cell lung cancer. *Eur. J. Nucl. Med. Mol. Imaging* **41**, 2058–2065 (2014).
34. Y.-J. Choi, B. C. Cho, Y. H. Jeong, H. J. Seo, H. J. Kim, A. Cho, J. H. Lee, M. Yun, T. J. Jeon, J. D. Lee, W. J. Kang, Correlation between ^{18}F-fluorodeoxyglucose uptake and epidermal growth factor receptor mutations in advanced lung cancer. *Nucl. Med. Mol. Imaging* **46**, 169–175 (2012).
35. X. Sun, G. Niu, Y. Yan, M. Yang, K. Chen, Y. Ma, N. Chan, B. Shen, X. Chen, Phage display–derived peptides for osteosarcoma imaging. *Clin. Cancer Res.* **16**, 4268–4277 (2010).
36. National Cancer Institute, Common Terminology Criteria for Adverse Events (CTCAE) version 4.0 (published on 14 June 2010).

Acknowledgments: **Funding:** This study was supported by the National Basic Research Program of China (2015CB931800), National Natural Science Foundation of China (81627901, 31210103913, and 81471724), Heilongjiang Province Foundation for Returned Overseas Chinese Scholars, and the Key Laboratory of Molecular Imaging Foundation (College of Heilongjiang Province). **Author contributions:** X.S. wrote the manuscript, in addition to designing, performing, and analyzing all experiments. Z.X., Z.H., Y. Liu, and C.Z. synthesized and characterized the tracer. G.C., Y. Sun, Y. Lin, and K.W. collected the information on NSCLC patients. Y. Song and C.Z. assisted with histology. F.F. and X.W. assisted with PET/CT imaging. L.X. and L. Shao assisted with the docking experiments. J.L. assisted with data analysis. S.S.G. and Z.C. assisted with experimental design, manuscript preparation, and data/image analysis. B.S. designed, supervised, and analyzed all experiments, in addition to assisting with manuscript preparation. **Competing interests:** ^{18}F-MPG synthesis (patent for B.S., X.S., Z.H., and Z.X.: The novel EGFR-TKIs F-MPG and H-MPG with antitumor activity and their preparation methods and application; ZL201610052162.9) and labeling methods (patent for B.S.: A fully automated one-step synthesis of ^{18}F-labeled 4-aminoquinazoline; ZL201310711309.7) that were used have been patented. The authors declare that they have no other competing interests. **Data and materials availability:** Patents have been filed concerning ^{18}F-MPG PET tracer preparation and imaging. These patents do not restrict the research or noncommercial use of the probe or technique. All data necessary to interpret the results are presented in the manuscript and the Supplementary Materials. The request for tracer/precursors should be handled through contacting of corresponding authors and a licensing agreement (for commercial purpose) or material transfer agreement (for research and noncommercial purposes).

Submitted 8 June 2017
Accepted 29 January 2018
Published 7 March 2018
10.1126/scitranslmed.aan8840

Citation: X. Sun, Z. Xiao, G. Chen, Z. Han, Y. Liu, C. Zhang, Y. Sun, Y. Song, K. Wang, F. Fang, X. Wang, Y. Lin, L. Xu, L. Shao, J. Li, Z. Cheng, S. S. Gambhir, B. Shen, A PET imaging approach for determining EGFR mutation status for improved lung cancer patient management. *Sci. Transl. Med.* **10**, eaan8840 (2018).

Science Translational Medicine

A PET imaging approach for determining EGFR mutation status for improved lung cancer patient management

Xilin Sun, Zunyu Xiao, Gongyan Chen, Zhaoguo Han, Yang Liu, Chongqing Zhang, Yingying Sun, Yan Song, Kai Wang, Fang Fang, Xiance Wang, Yanhong Lin, Lili Xu, Liming Shao, Jin Li, Zhen Cheng, Sanjiv Sam Gambhir and Baozhong Shen

Sci Transl Med **10**, eaan8840.
DOI: 10.1126/scitranslmed.aan8840

Tracing tumor treatment response

Tyrosine kinase inhibitors (TKIs) are a therapy for patients with non–small cell lung cancer (NSCLC) who have activating mutations in epidermal growth factor receptor (EGFR). To noninvasively detect tumor mutation status, Sun *et al*. designed a radiolabeled tracer for use with positron emission tomography and computed tomography imaging methods. The tracer identified tumors with activating mutant EGFR in rodent models of NSCLC and in patients with NSCLC. Patients with mutant EGFR had longer progression-free survival and responded to TKI therapy at a higher rate compared to patients with wild-type EGFR. This tracer could help identify patients with EGFR-TKI sensitivity and could be useful for monitoring response to treatment.

ARTICLE TOOLS	http://stm.sciencemag.org/content/10/431/eaan8840
SUPPLEMENTARY MATERIALS	http://stm.sciencemag.org/content/suppl/2018/03/05/10.431.eaan8840.DC1
RELATED CONTENT	http://stm.sciencemag.org/content/scitransmed/9/416/eaan6566.full http://stm.sciencemag.org/content/scitransmed/9/380/eaag0339.full http://stm.sciencemag.org/content/scitransmed/9/415/eaao4307.full http://stm.sciencemag.org/content/scitransmed/8/368/368ra172.full http://stm.sciencemag.org/content/scitransmed/5/216/216ra177.full http://stm.sciencemag.org/content/scitransmed/10/446/eaao2301.full http://stm.sciencemag.org/content/scitransmed/10/446/eaao2565.full http://stm.sciencemag.org/content/scitransmed/10/467/eaat5933.full
REFERENCES	This article cites 34 articles, 9 of which you can access for free http://stm.sciencemag.org/content/10/431/eaan8840#BIBL
PERMISSIONS	http://www.sciencemag.org/help/reprints-and-permissions

Use of this article is subject to the Terms of Service

Science Translational Medicine (ISSN 1946-6242) is published by the American Association for the Advancement of Science, 1200 New York Avenue NW, Washington, DC 20005. 2017 © The Authors, some rights reserved; exclusive licensee American Association for the Advancement of Science. No claim to original U.S. Government Works. The title *Science Translational Medicine* is a registered trademark of AAAS.

Downloaded from http://stm.sciencemag.org/ by guest on March 9, 2019